AGU ADVANCING EARTH AND SPACE SCIENCE

Geophysical Research Letters

RESEARCH LETTER
10.1029/2021GL093977

Low Velocity Zones in the Martian Upper Mantle Highlighted by Sound Velocity Measurements

F. Xu[1,2], N. C. Siersch[1], S. Gréaux[3], A. Rivoldini[4], H. Kuwahara[3,5], N. Kondo[3], N. Wehr[6], N. Menguy[1], Y. Kono[3], Y. Higo[7], A.-C. Plesa[8], J. Badro[6], and D. Antonangeli[1]

[1]Sorbonne Université, Muséum National d'Histoire Naturelle, UMR CNRS 7590, Institut de Minéralogie, de Physique des Matériaux et de Cosmochimie, IMPMC, Paris, France, [2]Now at Department of Earth Sciences, University College London, London, UK, [3]Geodynamics Research Center, Ehime University, Matsuyama, Japan, [4]Royal Observatory of Belgium, Brussels, Belgium, [5]Institute for Planetary Materials, Okayama University, Tottori, Japan, [6]Institut de physique du globe de Paris, CNRS, Université de Paris, Paris, France, [7]Japan Synchrotron Radiation Research Institute, Hyogo, Japan, [8]DLR Institute of Planetary Research, Berlin, Germany

Abstract The InSight mission to Mars is currently monitoring the seismic activity of the planet. Interpretation of seismological observations in terms of composition and mineralogy requires the knowledge of density and thermo-elastic properties of constituent materials at pertinent conditions. We thus performed phase equilibria experiments and carried out sound velocity and density measurements on aggregates representative of the Martian mantle over pressures and temperatures directly relevant for Mars' upper and mid mantle. Our results indicate the stability of magnetite, although in a small amount, in phase assemblages at upper mantle conditions, especially in an oxidized environment. The measured pressure and temperature derivatives of compressional and shear velocities show that the temperature-induced reduction of seismic wave speeds dominates over pressure-induced effects at Mars' shallow mantle conditions for the predicted areotherms and, independently from mineralogy, support the presence of a low-shear-wave-velocity layer between 150 and 350 km depth, in agreement with seismic observations.

Plain Language Summary The InSight mission operating on Mars is currently monitoring the planet's seismic activity. The recorded marsquakes can be used to obtain information on Mars' internal composition. However, the interpretation of these observations requires knowledge of the physical properties of the minerals expected to compose the Martian mantle at the relevant conditions. In this study we report: (1) experiments investigating the nature and abundance of the mineral phases stable at Martian mantle conditions; (2) sound velocity and density measurements on these rocks over a pressure and temperature range directly relevant for Mars' mantle, providing information that can be directly compared to the seismological findings from the InSight mission. Our results reveal the stability of small amounts of magnetite, an Fe^{3+}-rich mineral not reported in previous studies but a likely candidate in Mars' oxidized mantle environment. Moreover, measured wave velocities indicate the existence of a region between 150 and 350 km depth where, due to large temperature-induced reduction, shear wave velocities decrease with depth as opposed to an expected increase. This finding is consistent with recent observations from the InSight mission on Mars.

F. Xu and N. C. Siersch contributed equally to this work.

Key Points:

- Sound wave velocities and density were measured for pressures, temperatures, and mineralogical assemblages representative of Mars' mantle
- Experimental results support the existence of a low shear velocity layer in the shallow Martian mantle
- Phase equilibria experiments suggest the existence of ferrian minerals in the oxidized regions of the uppermost Martian mantle

Supporting Information:

Supporting Information may be found in the online version of this article.

Correspondence to:

D. Antonangeli,
daniele.antonangeli@upmc.fr

Citation:

Xu, F., Siersch, N. C., Gréaux, S., Rivoldini, A., Kuwahara, H., Kondo, N., et al. (2021). Low velocity zones in the Martian upper mantle highlighted by sound velocity measurements. *Geophysical Research Letters*, *48*, e2021GL093977. https://doi.org/10.1029/2021GL093977

Received 22 APR 2021
Accepted 13 SEP 2021

1. Introduction

The NASA's Discovery program mission InSight is the first mission, almost 40 years after the end of Viking 2 lander operations (Anderson et al., 1977), aiming at investigating the seismology of a rocky planetary body other than the Earth and the Moon. The spacecraft successfully landed on Mars in November 2018 (Banerdt et al., 2020), and since early winter 2019, its seismometer SEIS is continuously recording global seismic activity (Giardini et al., 2020). In the first year of operations, three quakes were strong enough to perform single station seismic analyses of Mars' subsurface and upper crust (Lognonné et al., 2020; Knapmeyer-Endrun et al., 2021). Observations of direct and reflected body-wave phases from these and few other marsquakes have been used to provide first constraints on seismic structure to a depth of 800 km (Khan et al., 2021) and the size of the core (Stähler et al., 2021). However, in order to invert seismic models for information on the composition and mineralogy of Mars' interior, knowledge of the sound velocities and density of relevant

minerals and mineralogical assemblages at pertinent thermodynamic conditions are critically needed. Furthermore, most of the Martian seismic data available so far do not allow for independent source localization (Giardini et al., 2020), and a-priori knowledge of sound velocity variations as a function of pressure and temperature would play an essential role in interpreting the nature and depths of the observed seismic events. Self-consistent thermodynamic mineralogy and seismic wave velocity models of the Martian mantle have been computed for a series of pressure-temperature profiles and for a selection of bulk chemical compositions (Smrekar et al., 2019 and references therein) along self-consistent adiabats by Gibbs free-energy minimization (Connolly, 2009) using the thermodynamic formulation of Stixrude and Lithgow-Bertelloni (2005, 2011). While internally consistent, these calculations rely on available thermodynamic databases (e.g., Holland et al., 2013; Stixrude & Lithgow-Bertelloni, 2011), which have been largely constructed on the basis of minerals with compositions relevant to Earth's mantle. Experiments and calculations have not yet sufficiently constrained the thermoelastic properties of Fe-rich end members, especially Fe^{3+}-rich, minerals across the full range of pressure and temperature of Mars' mantle. Since Mars' mantle is believed to be especially enriched in Fe (Fe# = [Fe/(Fe + Mg)] × 100 = 25, e.g., Dreibus & Wänke, 1985) compared to Earth's mantle (Fe# = 10, e.g., Takahashi, 1986), potentially with oxidized regions in its uppermost part (Tuff et al., 2013), current estimations do not encompass the full range of possibilities, and proposed velocity models are based on, and possibly biased by, an incomplete dataset.

The only experimental study so far investigating the phase assemblages of Mars' mantle has been performed by Bertka and Fei (1997). The synthetized aggregates at Mars' upper mantle conditions were predominantly made of olivine and pyroxene down to ~200 km depth corresponding to ~2 GPa. From this depth, pyroxene dissolves into garnet through the entire upper mantle, until olivine transforms into wadsleyite at ~1,100 km depth (13.5 GPa), marking the beginning of the Martian counterpart of the transition zone as defined for the Earth's mantle (Bertka & Fei, 1997). The compositions of the olivine and pyroxene phases measured by Bertka and Fei (1997) were found to be characterized by 25 mol.% of the respective Fe end-member. Despite the reducing conditions in the experiments (both of the starting material and synthesis setup), the garnets present in the assemblages representative of the upper mantle contain not only 21 mol.% of almandine ($Fe^{2+}_3Al_2Si_3O_{12}$) component but also 5 mol.% of the skiagite ($Fe^{2+}_3Fe^{3+}_2Si_3O_{12}$) component, the latter being a Fe^{3+}-rich end-member of garnet whose thermoelastic properties have not been studied in much detail, especially lacking high-temperature data (Ismailova et al., 2017; Vasiukov et al., 2018; Woodland et al., 1999). Since Mars is believed to have oxidized regions at least in the uppermost mantle (Tuff et al., 2013), studying more oxidizing conditions during phase equilibria experiments in order to obtain mineralogical assemblages, which are potentially more representative of the Martian mantle, is essential.

Here, we measured the bulk compressional (v_P) and shear (v_S) wave velocities as well as densities of representative Martian upper mantle mineral aggregates synthesized at various redox conditions by means of in situ ultrasonic experiments combined with synchrotron radiation at pressures and temperatures relevant to the Martian upper mantle. Our results provide direct guidance to the interpretation of seismic observations and extend on available datasets for thermodynamic models.

2. Materials and Methods

Homogeneous spherical glass samples (diameter ~2.5–3 mm) were produced in an aerodynamic levitation laser furnace, by fusing a powder mixture with bulk composition close to the one proposed by Taylor (2013) (oxides expected to be present at a level below 1 wt.% were not included in the starting material), employing different gas mixtures (Ar, CO_2, H_2), and quenching the melt. The glass spheres were then polished to cylinder shapes and re-equilibrated in a multi-anvil or a piston-cylinder press, to crystallize phase assemblages analogous of the Martian mantle at high pressure and temperature (UM1 at 3 GPa and 1373 K; UM2 at 3 GPa and 1473 K; MM1 at 8 GPa and 1473 K, see Table S1). All recovered samples were well sintered. Assemblages were further analyzed using a scanning electron microscope (SEM) and electron microprobe (EMP)/transmission electron microscope (TEM) to determine grain size, mineral phases, and compositions (Tables 1 and S1). For more detailed information, please refer to the Supporting Information S1.

Sound wave velocity and density measurements were carried out at the beamline BL04B1, SPring-8, Japan, in three in situ experiments using combined ultrasonic interferometry, X-ray radiography and X-ray

Table 1
Phase Proportions of Measured Samples and Compositions of Constituent Phases

Run NO.	Ol	Opx[a]	Gt	Mag	Bulk (1)	Bulk (2)
UM1 (TEM) 3 GPa, 1,373K, 1 h[b]						
SiO_2	39.0	53.2		1.4	45.7	43.2
Al_2O_3	–	3.7		10.0	3.2	2.2
FeO[c]	21.1	11.8		24.1	19.3	17.1
Fe_2O_3[c]	–	1.9		59.1	–	4.1
MgO	39.8	27.4		5.3	29.7	32.4
CaO	0.1	2.0		0.1	2.0	1.0
UM2 (EMP) 3 GPa, 1,473K, 24 h						
SiO_2	39.4	50.9		1.6	46.4	42.4
Al_2O_3	0.5	4.3		14.3	3.3	3.0
FeO	20.6	7.7		21.2	18.1	14.9
Fe_2O_3	–	6.9		55.2	–	6.1
MgO	39.0	28.3		7.5	29.5	32.5
CaO	0.5	1.9		0.1	2.8	1.1
MM1[d] (EMP) 8 GPa, 1,473K, 23 h						
SiO_2	39.1	55.7	40.3		45.8	44.3
Al_2O_3	0.2	0.5	10.9		3.3	2.9
FeO	21.1	11.3	8.8		18.6	15.3
Fe_2O_3	–	1.3	17.1		–	4.4
MgO	39.2	30.0	15.9		29.8	31.0
CaO	0.4	1.2	6.9		2.5	2.2
Phase proportion						
UM1	44	50		6		
UM2	43	54		3		
MM1	47	30	23			

Note. The bulk composition of each sample is estimated in two different ways: (1) by SEM analysis performed over large window scans (200 × 200 μm) and averaged over multiple areas of the sample; and (2) from the phase proportions determined from the SEM/TEM images and compositions of each phase. In case (1) all Fe is counted as FeO. The starting chemical composition of oxide mixture is in wt.% SiO_2: 44.6; Al_2O_3: 3.1; FeO: 18.5; MgO: 31.2; CaO: 2.5. Phases are olivine (Ol), orthopyroxene (Opx), garnet (Gt), and magnetite (Mag).

[a]Only orthopyroxene was counted here due to the non-detection of clinopyroxene in SEM and EMP measurement. (see also Table S3). [b]The TEM or EMP in the parathesis indicate the composition was obtained by TEM or EMP analysis, respectively. Pressure, temperature, and duration of the synthesis run are also indicated. [c]The valence states iron in Opx, Gt, and Mag was calculated according to the charge balance method (Quinn et al., 2016). See S2 in Supporting Information S1 for more details. [d]Composition was measured after synthesis, before sound wave velocity measurement.

diffraction under high-pressure and high-temperature. Measurements have been conducted up to 6.8(1) GPa and 900 K for the upper mantle assemblages, and up to 10.6(1) GPa and 1200 K for the mid-mantle assemblage (see Supporting Information S1 and Figure S1). The two-way travel time (t) was measured by the pulse echo method, analyzing the time delay between the buffer and sample echoes (Figure S2). At each pressure and temperature, the sample length (L) was measured by X-ray radiography, imaging two gold foils placed at both ends of the sample (Figure S3), and the compressional and shear wave velocities were calculated using the relation $= \frac{2L}{t}$. The pressure and temperature dependences of each mineralogical assemblage were derived by global fitting the respective P-T-v_P-v_S datasets to a linear function following:

$$v_{P,S} = v_{0P,S} + \partial\left(v_{P,S}\right)/\partial P * P + \partial\left(v_{P,S}\right)/\partial T * \left(T - 300K\right)$$

(see also Figure S4).

Energy-dispersive diffraction patterns were collected for both the samples (Figure S5) and pressure marker using a solid-state Ge-detector at a fixed 2θ angle of ~6°. The unit-cell volumes of the Au pressure marker were used to determine the pressure at each temperature point according to the P-V-T equation of state of gold (Tsuchiya, 2003). The unit-cell parameters of olivine, orthopyroxene, garnet and magnetite, if detected (Table S2), were determined using full profile LeBail refinements within the GSAS software package in the EXPGUI interface (Larson & Von Dreele, 2004; Toby, 2001).

3. Results and Discussion

The three aggregates show distinct mineralogies, mainly differing in proportions of olivine, pyroxene, garnet, and, when present, magnetite (Figure S6). The phase assemblages equilibrated at Martian upper mantle P–T conditions (UM1 and UM2) are comparable in terms of phase proportions and compositions (Table 1), with 50–54 vol.% olivine, 43–44 vol.% orthopyroxene and 3–6 vol.% magnetite, as determined from analysis of SEM and TEM images (see Supporting Information S1). Differently from the results of Bertka and Fei (1997), garnet is absent in these samples due to the stabilization of magnetite (Table S3). Clinopyroxene shows a small grain size, i.e., <500 nm, making it only observed in TEM composition mapping but not detectable by SEM and EPMA measurements (Tables 1 and S3). The Fe# of olivine in both assemblages is identical (Fe# = 23), whereas in orthopyroxene, the Fe# of UM1 is 20 compared to a Fe# = 22 in UM2, which can be attributed to the fact that 3 vol.% more Al-Mg-rich magnetite is present in UM1 than in UM2 incorporating some amount of Fe into its structure. Magnetite is observed in these upper mantle assemblages irrespective of the gas flux used in the glass synthesis and the capsule material used for the high P-T equilibrations (Table S1), and this is another major difference with respect to the previous study by Bertka and Fei (1997) (Table S3). One possible explanation is the use of Re and Pt foils and the Fe^{3+}-rich oxide mixtures as starting material in this study, in contrast to the more reducing conditions imposed by the capsule materials (graphite-lined Pt capsules) containing the previously reduced starting material used by Bertka and Fei (1997). Noteworthy, a recent study reported the stability of magnetite next to majoritic garnet and pyroxene when starting from a bulk composition similar to the one investigated here (Tao et al., 2018). More

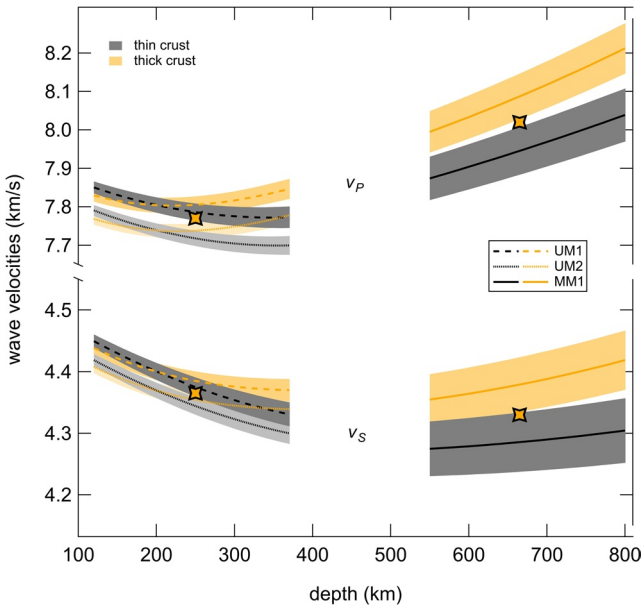

Figure 1. Experiment-based compressional v_P and shear wave velocities v_S of three different mineralogical assemblages versus depth along two different areotherms. The black and orange lines represent the two areotherms assuming a thin crust (Case 12, 45 km) or thick crust (Case 56, 87.1 km), respectively. Extended low-velocity zones are visible for v_S in both cases. V_P shows a low-velocity zone only for the thin crust areotherm (Case 12). The shaded areas represent the experimental uncertainties. Results are for constant mineralogy, corresponding to equilibrium mineralogy at depth ~250 km (UM1 and UM2) and ~650–680 km (MM1), indicated as stars in the figure.

importantly, the presence of Fe^{3+} bearing phases, and possibly magnetite, in the Martian mantle assemblage is reasonable under the assumption of an Fe-rich and oxidized uppermost mantle (Tuff et al., 2013). Still, ferrian minerals have not been taken into account in any of the mineralogy and velocity models considered so far (e.g., Smrekar et al., 2019 and references therein).

The phase assemblage of the run under mid-mantle *P*–*T* condition (MM1) contains 23 vol.% of garnet, 30 vol.% of orthopyroxene and 47 vol.% of olivine (Table 1). The Fe# in olivine and orthopyroxene are 23 and 18, respectively, with the garnet being rich in Fe^{3+}, containing 23 mol.% skiagite ($Fe^{2+}{}_3Fe^{3+}{}_2Si_3O_{12}$) and 18 mol.% andradite ($Ca_3Fe^{3+}{}_2Si_3O_{12}$) components. Such an enrichment in Fe^{3+} is significant, especially if compared to the previous phase equilibrium study (Bertka & Fei, 1997).

The compressional and shear wave velocities for all three runs increase monotonically with pressure and decrease with increasing temperatures (e.g., UM2 in Figure S4). Both v_P and v_S for the upper mantle experiments UM1 and UM2 are very similar, within mutual uncertainties (Table S4). This observation can be readily explained in view of the similar phase assemblages and mineralogy of the two samples. The wave velocities v_P and v_S for the mid-mantle experiment MM1 are higher than those measured for the upper mantle experiments (Table S4) and with a larger increase with increasing pressure, presumably related to the presence of garnet in this phase assemblage (Table S1).

Using the derivatives of v_P and v_S with respect to *T* and *P* from the experimental dataset of this study (Table S5), v_P and v_S of each phase assemblage are calculated as a function of depth along two different Martian mantle temperature profiles (areotherms) (Figure 1). These areotherms are chosen as representative cases out of a larger series established by recent 3-D thermal evolution models (Plesa et al., 2018). Both areotherms have been calculated assuming a crustal heat production rate compatible with the surface abundance of heat producing elements measured by the gamma ray spectrometer instrument onboard Mars Odyssey (Hahn et al., 2011; Taylor et al., 2006). Case 12 is representative for a relatively thin crust (45 km) that contains about 44% of the total bulk amount of heat producing elements and is characterized by a steep temperature increase down to depths of ~350 km, from where the temperature profile flattens out toward the lower mantle (Figure S7). Case 56 considers a thick crust (87.1 km) that contains most of the heat producing elements, i.e., 94%, leading to an overall less pronounced temperature increase at shallow depths. In this latter case, the areotherm starts flattening out at a depth of 800 km reaching a temperature approximately 420 K lower compared to Case 12 (Figure S7). From our experimental data, we predict a low-velocity layer, i.e., a decrease in wave velocities with increasing depth, at shallow mantle depths (~150–350 km depths range) for both v_P and v_S for the thin-crust areotherm (Case 12). For the thick-crust areotherm (Case 56), a low-velocity layer is present for v_S, whereas variation of v_P with depth (initial small reduction followed by a slight increase) are too small to derive firm conclusions. Results along more areotherms for thin and thick crust and different thermal evolution models (Plesa et al., 2018) are shown in the Supporting Information S1 (Figure S8). Different temperature profiles affect absolute values of velocities, but not the overall behavior with depth for the two classes of areotherms (i.e., thin and thick crust). The occurrence of extended low-shear-velocity zones is predicted for all phase assemblages considered here and can be explained by the temperature-induced velocity decrease prevailing over the pressure-induced velocity increase at depths shallower than 400 km.

The obtained experimental results along the Case 12 areotherm are compared to wave velocities modeled along the same areotherm for aggregates having the same bulk composition of the experiments but assuming all Fe to be present as Fe^{2+} due to the absence of Fe^{3+} in end-member phases in the Stixrude and Lithgow-Bertelloni (2011) database (Figure 2). Specifically, equilibrium phase assemblages are determined

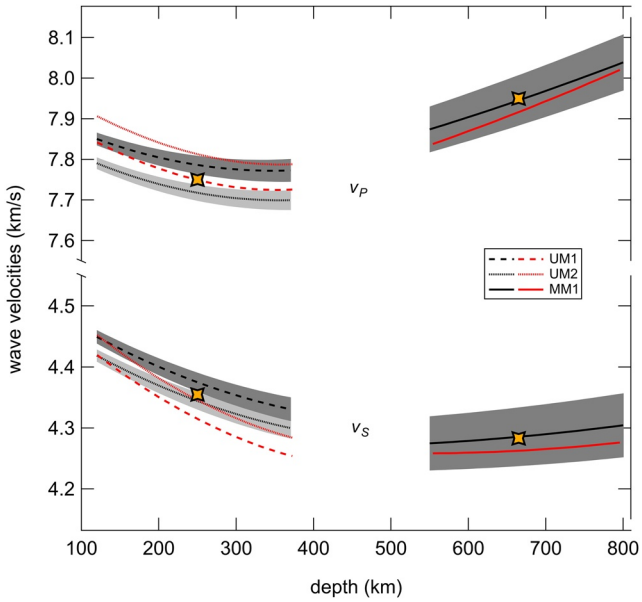

Figure 2. Experiment-based compressional v_P and shear wave velocities v_S of three different mineralogical assemblages versus depth along a thin crust areotherm (Case 12, 45 km average crustal thickness, black) in comparison to velocities according to thermodynamic calculations (red lines). The modeled velocities were calculated using the thermodynamic formulation of Stixrude and Lithgow-Bertelloni (2005) and parameters of Stixrude and Lithgow-Bertelloni (2011) for composition Bulk (2) (see Table 1), but assuming all Fe to be present as Fe^{2+} due to the absence of Fe^{3+} in end-member phases in the Stixrude and Lithgow-Bertelloni (2011) database. Calculations for composition Bulk (1) differ at most by 0.05 km/s for v_P and 0.03 km/s for v_S. The shaded areas represent the experimental uncertainties. Noteworthy, while experimental results are for constant mineralogy, corresponding to equilibrium mineralogy at depth ~250 km (UM1 and UM2) and ~650–680 km (MM1), indicated as stars in the figure, thermodynamic models have mineralogy resulting from Gibbs free-energy minimization and thus evolving with depth.

by Gibbs free energy minimization using Perple_X (Connolly, 2009) (Table S3), and the elastic properties of the aggregates are computed with the thermodynamic formulation and thermodynamic database of Stixrude and Lithgow-Bertelloni (2005, 2011). The overall agreement between experiment-based velocity profiles and models is good, in particular for the mid-mantle assembly, where the two are within uncertainties. For upper-mantle assemblies modeled, v_P is below (UM1) or above (UM2) experiment-based velocity profiles by ~1%, while v_S is below by ~2% in the case of UM1 or close for UM2. Accordingly, neglecting the presence of Fe^{3+} bearing minerals leads to less than 2% difference between the results obtained in our experiments and self-consistent thermodynamic models.

The experimental results along the areotherm Case 12 are also compared to mantle velocity models (Smrekar et al., 2019) computed along the same areotherm using the thermodynamic approach detailed above (Figure 3a). Several bulk chemistry compositions proposed for the mantle of Mars are considered here—MA: Morgan & Anders, 1979; LF: Lodders & Fegley, 1997; EH45 and EH70: Sanloup et al., 1999; MM: Mohapatra & Murty, 2003; TA: Taylor, 2013; and YO: Yoshizaki & McDonough, 2020; together with the bulk chemistry of our starting material (Table 1). It is important to note that the experiment-based results are computed for constant mineralogy, corresponding to equilibrium mineralogy at depth ~250 km (UM1 and UM2) and ~650–680 km (MM1). Thermodynamic models use Gibbs free-energy minimization and thus have a mineralogy that evolves with depth. Both v_P and v_S obtained from the ultrasonic experiments and modeled for our starting composition plot on the lower end of the velocities calculated with thermodynamic models, close to estimations for the composition EH70 suggested by Sanloup et al. (1999), despite the significant difference in major element concentration (+7.3 wt.% SiO_2; −0.53 wt.% Al_2O_3, −6.7 wt.% FeO, −3.2 wt.% MgO and −0.43 wt.% CaO of EH70 with respect to our composition). Assuming the areotherm Case 56, both the experimental and calculated wave velocities increase slightly, without changes to the relative difference. Overall, we observe generally faster wave velocities from the previously published models compared to our experiments and model. The TA model, which has a bulk chemistry very close to that of our experiments, shows a v_P/v_S ratio very close to that modeled for our starting composition (Figure 3b) but absolute velocities systematically above our measurements (difference up to ~0.23 km/s and up to ~0.1 km/s for v_P and v_S, respectively). This offset can be explained by the larger amounts of clinopyroxene in the TA model (up to 19.1%) and less orthopyroxene (13.3%) compared to the phase proportion modeled for the starting material composition of this study, resulting in the stability of only 5.6% of clinopyroxene and a larger amount of orthopyroxene (up to 28.2%) (Table S3). Indeed, at pressure and temperature conditions of the Case 12 areotherm clinopyroxene is faster compared to orthopyroxene (Flesch et al., 1998; Kung et al., 2005, 2011; Li & Neuville, 2010). In comparison to a typical mineralogy of the Earth's mantle (Ringwood, 1969), calculated along the same areotherms (Figure 3a), the wave velocities through Mars' upper and mid-mantle are significantly slower than those of the Earth, ~0.5 km/s for v_P and ~0.3 km/s for v_S. This can be attributed not only to the higher garnet and olivine over pyroxene content in the Earth but also to the lower Fe# of ~10 assumed for the Earth versus a Fe# of ~25 expected for Mars, which has a significant effect on the bulk wave velocities (Stixrude & Lithgow-Bertelloni, 2011).

Irrespective of absolute velocity values, a low-S-wave-velocity layer at shallow depths is expected according to both experiments and for all self-consistent thermodynamic models, further supporting the independence of this finding from mineralogy. Available Martian seismic records suggest a possible S-wave shadow zone at an epicentral distance range of ~40–60° from the InSight landing site (Giardini et al., 2020; Khan et al., 2021), which might result from the presence of a low-velocity layer in the upper mantle.

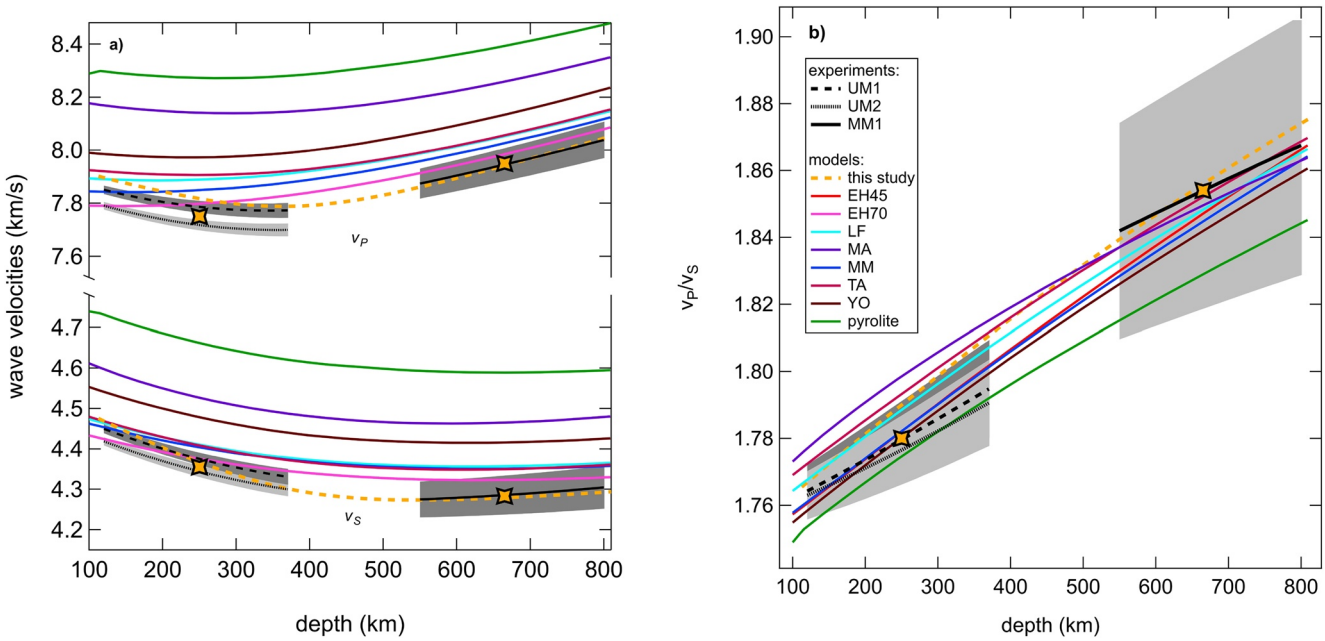

Figure 3. Experiment-based compressional v_P and shear wave velocities v_S (a) and v_P/v_S (b) of three different mineralogical assemblages studied here versus depth along the thin crust areotherm Case 12 (45 km average crustal thickness). The gray shaded areas represent the experimental uncertainties. Self-consistent thermodynamic models (colored lines) calculated for different bulk starting compositions proposed in literature show wave velocities faster than the experimental ones. We note, however, that experimental results are for constant mineralogy, corresponding to equilibrium mineralogy at depth ~250 km (UM1 and UM2) and ~650–680 km (MM1), indicated as stars in the figure, while self-consistent thermodynamic models have been computed for mineralogy evolving with depth.

Our experimental results and the above-presented considerations provide a direct explanation for this observation and support the existence of a low-S-wave-velocity zone in the upper mantle of Mars (Khan et al., 2021) as a direct consequence of the dominant temperature-induced effects on seismic velocities along all areotherms considered in this study (Plesa et al., 2018). Whether or not a low-P-wave-velocity layer will be observed on Mars would provide constraints on the thermal structure of the upper mantle, with a low-P-wave-velocity zone being a strong indication of hot temperatures in the shallow mantle, such as the temperature profile Case 12 of Plesa et al. (2018).

The v_P/v_S ratio between 100 and 800 km depth, which directly affects the difference in the arrivals between P-waves and S-waves, is shown in Figure 3b. This ratio shows a smooth monotonic increase for all three Martian compositions investigated in this study. Within experimental uncertainties, shown as shaded areas, v_P/v_S is the same for the two upper mantle assemblages. Furthermore, the experimental data clearly fall into the same range as calculated for different Martian compositions using thermodynamic end-member data by Stixrude and Lithgow-Bertelloni (2011). Compared to a typical v_P/v_S for Earth's mantle composition (Ringwood, 1969) along a Martian temperature profile, the bulk v_P/v_S for Mars is larger, especially for depths >400 km. Another interesting observation is that the dependence of v_P/v_S on pressure in our assemblages does not significantly vary along isotherms, for temperatures in the range of 300–2500 K tested by extrapolation of results in this study. Thus, the measured v_P/v_S ratio provides important constraints for the estimation of the epicentral distance of marsquakes recorded by InSight.

4. Conclusions

In this study, we report the stability of magnetite, although to a small fraction, in Martian mantle phase assemblages at conditions directly pertinent to its upper mantle, especially in an oxidized environment. Additionally, the presence of Fe^{3+}-bearing garnets was inferred in the mid-mantle phase assemblage. We thus argue for a Martian mantle mineralogy more complex compared to what has been considered so far (e.g., Bertka & Fei, 1997; Smrekar et al., 2019 and references therein). Sound velocity measurements have

been carried out at high pressure and high temperature and suggest seismic wave velocities possibly slower compared to the majority of the velocity models that have been previously proposed for Mars. Whether the difference between experiments and thermodynamic models is the result of the presence of iron as Fe^{3+} or of the different phase proportions in our assemblages compare to those predicted by existing thermodynamic equilibrium calculations remains to be assessed. Nevertheless, the presence of a low-S-wave-velocity layer extending between 150 and 350 km depth, and possibly up to ~500 km depth, is independent of the considered mineralogy and thermal structure and is therefore a robust conclusion that is compatible with the findings from recent InSight seismic observations (Giardini et al., 2020; Khan et al., 2021). The v_P/v_S ratio depends only weakly on mantle composition and mineralogy and is largely independent of temperature. Hence, the v_P/v_S ratio that has been measured in this study provides direct constraints for the estimation of the epicentral distance of quakes and guidance for the interpretation of seismic data collected on Mars.

Acknowledgments
We thank two anonymous reviewers for their thoughtful and constructive comments that have improved an earlier version of this paper. We also thank the editor A. J. Dombard for handling the revision process of the manuscript. The authors wish to thank Imène Estève and Stéphanie Delbrel for their help with ion-milling and sample analysis by SEM at the Institut de Minéralogie de Physique des Matériaux et de Cosmochimie (IMPMC, Paris) and Michel Fialin and Nicolas Rividi for their help during microprobe analysis at the Centre Camparis, Sorbonne Université (Paris, France). We would like to thank Stephan Borensztajn for his help with the FIB cutting at IPGP (Paris, France). This project has received funding from the European Research Council (ERC) under the European Union's Horizon 2020 research and innovation Programme (Grant Agreement 724690). This work was supported by the French Space Agency (CNES), focused on SEIS instrument of the InSight mission. AR is financially supported by the Belgian PRODEX program managed by the European Space Agency in collaboration with the Belgian Federal Science Policy Office. ACP gratefully acknowledges the financial support and endorsement from the DLR Management Board Young Research Group Leader Program and the Executive Board Member for Space Research and Technology. The Focused Ion Beam (FIB) and Scanning Electron Microscope (SEM) facility at IMPMC is supported by Région Ile de France Grant SESAME 2006 N°I-07-593/R, INSU-CNRS, Institute de Physique (INP)–CNRS, University Pierre et Marie Curie–Paris 6, and by the French National Research Agency (ANR) Grant ANR-07-BLAN-0124-01. Infrastructures and services at the Geodynamics Research Center (GRC), Ehime University, were made available through the PRIUS program. The synchrotron radiation experiments were performed under SPring-8 Non-Proprietary Research Proposals Numbers 2019A1473 and 2019B1305, in collaboration with the partner user program (2019A0069 and 2019B0069). This paper is InSight Contribution 199.

Data Availability Statement

Datasets for this research (main paper and Supporting Information S1) are available at https://doi.org/10.5281/zenodo.4709036 (doi: 10.5281/zenodo.4709036).

References

Anderson, D. L., Miller, W. F., Latham, G. V., Nakamura, Y., Toksöz, M. N., Dainty, A. M., et al. (1977). Seismology on Mars. *Journal of Geophysical Research*, *82*, 4524–4546. https://doi.org/10.1029/JS082i028p04524

Banerdt, W. B., Smrekar, S. E., Banfield, D., Giardini, D., Golombek, M., Johnson, C. L., et al. (2020). Initial results from the InSight mission on Mars. *Nature Geoscience*, *13*(3), 183–189. https://doi.org/10.1038/s41561-020-0544-y

Bertka, C. M., & Fei, Y. (1997). Mineralogy of the Martian interior up to core-mantle boundary pressures. *Journal of Geophysical Research: Solid Earth*, *102*(B3), 5251–5264. https://doi.org/10.1029/96jb03270

Connolly, J. A. D. (2009). The geodynamic equation of state: What and how. *Geochemistry, Geophysics, Geosystems*, *10*(10). https://doi.org/10.1029/2009GC002540

Dreibus, G., & Wänke, H. (1985). Mars, a volatile-rich planet. *Meteoritics*, *20*(2), 367–381.

Flesch, L. M., Li, B., & Liebermann, R. C. (1998). Sound velocities of polycrystalline MgSiO3-orthopyroxene to 10 GPa at room temperature. *American Mineralogist*, *83*(5–6), 444–450.

Giardini, D., Lognonné, P., Banerdt, W. B., Pike, W. T., Christensen, U., Ceylan, S., et al. (2020). The seismicity of Mars. *Nature Geoscience*, *13*(3), 205–212. https://doi.org/10.1038/s41561-020-0539-8

Hahn, B. C., McLennan, S. M., & Klein, E. C. (2011). Martian surface heat production and crustal heat flow from Mars Odyssey gamma-ray spectrometry. *Geophysical Research Letters*, *38*, L14203. https://doi.org/10.1029/2011GL047435

Holland, T. B., Hudson, N. F. C., Powell, R., & Harte, B. (2013). New thermodynamic models and calculated phase equilibria in NCFMAS for basic and ultrabasic compositions through the transition zone into the uppermost lower mantle. *Journal of Petrology*, *54*(9), 1901–1920. https://doi.org/10.1093/petrology/egt035

Ismailova, L., Bykov, M., Bykova, E., Bobrov, A., Kupenko, I., Cerantola, V., et al. (2017). Effect of composition on compressibility of skiagite-Fe-majorite garnet. *American Mineralogist*, *102*(1), 184–191. https://doi.org/10.2138/am-2017-5856

Khan, A., Ceylan, S., van Driel, M., Giardini, D., Lognonné, P., Samuel, H., et al. (2021). Upper mantle structure of Mars from InSight seismic data. *Science*, *373*, 434–438. https://doi.org/10.1126/science.abf2966

Knapmeyer-Endrun, B., Panning, M., Bissig, F., Joshi, R., Khan, A., Kim, D., et al. (2021). Thickness and structure of the Martian crust from InSight seismic data. *Science*, *373*, 438–443. https://doi.org/10.1126/science.abf8966

Kung, J., Jackson, I., & Liebermann, R. C. (2011). High-temperature elasticity of polycrystalline orthoenstatite (MgSiO 3). *American Mineralogist*, *96*(4), 577–585. https://doi.org/10.2138/am.2011.3632

Kung, J., Li, B., Uchida, T., & Wang, Y. (2005). In-situ elasticity measurement for the unquenchable high-pressure clinopyroxene phase: Implication for the upper mantle. *Geophysical Research Letters*, *32*(1), 1–4. https://doi.org/10.1029/2004GL021661

Larson, A. C., & Von Dreele, R. B. (2004). *General structure analysis system (GSAS)* (pp. 86–748). Los Alamos National Laboratory Report. Report.

Li, B., & Neuville, D. R. (2010). Elasticity of diopside to 8GPa and 1073K and implications for the upper mantle. *Physics of the Earth and Planetary Interiors*, *183*(3–4), 398–403. https://doi.org/10.1016/j.pepi.2010.08.009

Lodders, K., & Fegley, B. (1997). An oxygen isotope model for the composition of Mars. *Icarus*, *126*(2), 373–394. https://doi.org/10.1006/icar.1996.5653

Lognonné, P., Banerdt, W. B., Pike, W. T., Giardini, D., Christensen, U., Garcia, R. F., et al. (2020). Constraints on the shallow elastic and anelastic structure of Mars from InSight seismic data. *Nature Geoscience*, *13*(3), 213–220. https://doi.org/10.1038/s41561-020-0536-y

Mohapatra, R. K., & Murty, S. V. S. (2003). Precursors of Mars: Constraints from nitrogen and oxygen isotopic compositions of martian meteorites. *Meteoritics and Planetary Science*, *38*(2), 225–241. https://doi.org/10.1111/j.1945-5100.2003.tb00261.x

Morgan, J. W., & Anders, E. (1979). Chemical composition of Mars. *Geochimica et Cosmochimica Acta*, *43*(10), 1601–1610. https://doi.org/10.1016/0016-7037(79)90180-7

Plesa, A. C., Padovan, S., Tosi, N., Breuer, D., Grott, M., Wieczorek, M. A., et al. (2018). The thermal state and interior structure of Mars. *Geophysical Research Letters*, *45*(22), 12,198-12,209. https://doi.org/10.1029/2018GL080728

Quinn, R. J., Valley, J. W., Page, F. Z., & Fournelle, J. H. (2016). Accurate determination of ferric iron in garnets. *American Mineralogist*, *101*, 1704–1707. https://doi.org/10.2138/am-2016-5695

Ringwood, A. E. (1969). Composition of the crust and upper mantle. The Earth's Crust and Upper Mantle, *Geophysical Monograph Series*, *13*, 1–17.

Sanloup, C., Jambon, A., & Gillet, P. (1999). A simple chondritic model of Mars. *Physics of the Earth and Planetary Interiors*, *112*(1–2), 43–54. https://doi.org/10.1016/S0031-9201(98)00175-7

Smrekar, S. E., Lognonné, P., Spohn, T., Banerdt, W. B., Breuer, D., Christensen, U., et al. (2019). Pre-mission InSights on the Interior of Mars. *Space Science Reviews*, *215*, 1–72. https://doi.org/10.1007/s11214-018-0563-9

Stähler, S. C., Khan, A., Banerdt, W. B., Lognonné, P., Giardini, D., Ceylan, S., et al. (2021). Seismic detection of the Martian core. *Science*, *373*, 443–448. https://doi.org/10.1126/science.abi7730

Stixrude, L., & Lithgow-Bertelloni, C. (2005). Thermodynamics of mantle minerals - I. Physical properties. *Geophysical Journal International*, *162*(2), 610–632. https://doi.org/10.1111/j.1365-246X.2005.02642.x

Stixrude, L., & Lithgow-Bertelloni, C. (2011). Thermodynamics of mantle minerals - II. Phase equilibria. *Geophysical Journal International*, *184*(3), 1180–1213. https://doi.org/10.1111/j.1365-246X.2010.04890.x

Takahashi, E. (1986). Melting of a dry peridotite KLB-1 up to 14 GPa: Implications on the origin of peridotitic upper mantle. *Journal of Geophysical Research*, *91*(B9), 9367. https://doi.org/10.1029/jb091ib09p09367

Tao, R., Fei, Y., Bullock, E. S., Xu, C., & Zhang, L. (2018). Experimental investigation of Fe3+-rich majoritic garnet and its effect on majorite geobarometer. *Geochimica et Cosmochimica Acta*, *225*, 1–16. https://doi.org/10.1016/j.gca.2018.01.008

Taylor, G. J. (2013). The bulk composition of Mars. *Chemie der Erde*, *73*(4), 401–420. https://doi.org/10.1016/j.chemer.2013.09.006

Taylor, G. J., Boynton, W., Brückner, J., Wänke, H., Dreibus, G., Kerry, K., et al. (2006). Bulk composition and early differentiation of Mars. *Journal of Geophysical Research*, *111*, E03S10. https://doi.org/10.1029/2005JE002645

Toby, B. H. (2001). EXPGUI, a graphical user interface for GSAS. *Journal of Applied Crystallography*, *34*(2), 210–213. https://doi.org/10.1107/S0021889801002242

Tsuchiya, T. (2003). First-principles prediction of the P - V - T equation of state of gold and the 660-km discontinuity in Earth's mantle. *Journal of Geophysical Research: Solid Earth*, *108*(B10), 311–328. https://doi.org/10.1029/2003jb002446

Tuff, J., Wade, J., & Wood, B. J. (2013). Volcanism on Mars controlled by early oxidation of the upper mantle. *Nature*, *498*(7454), 342–345. https://doi.org/10.1038/nature12225

Vasiukov, D. M., Ismailova, L., Kupenko, I., Cerantola, V., Sinmyo, R., Glazyrin, K., et al. (2018). Sound velocities of skiagite–iron–majorite solid solution to 56 GPa probed by nuclear inelastic scattering. *Physics and Chemistry of Minerals*, *45*(5), 397–404. https://doi.org/10.1007/s00269-017-0928-8

Woodland, A. B., Angel, R. J., Koch, M., Kunz, M., & Miletich, R. (1999). Equations of state for Fe 3 2+ Fe 2 3+ Si 3 O 12 "skiagite" garnet and Fe_2 SiO_4 -Fe_3O_4 spinel solid solutions. *Journal of Geophysical Research: Solid Earth*, *104*(B9), 20049–20058. https://doi.org/10.1029/1999jb900206

Yoshizaki, T., & McDonough, W. F. (2020). The composition of Mars. *Geochimica et Cosmochimica Acta*, *273*, 137–162. https://doi.org/10.1016/j.gca.2020.01.011